

# Fast Huygens sweeping methods for multi-arrival Green's Functions of Helmholtz equations in the high frequency regime

Jianliang Qian<sup>1</sup>, Songting Luo<sup>2</sup>, and Robert Burridge<sup>3</sup>

<sup>1</sup> *Department of Mathematics, Michigan State University, East Lansing, MI 48824. Email:*

**qian@math.msu.edu**

<sup>2</sup> *Department of Mathematics, Iowa State University, Ames, IA 50011. Email:*

**luos@iastate.edu**

<sup>3</sup> *Department of Mathematics and Statistics, University of New Mexico, Albuquerque, NM 87131.*

*Email: burridge137@gmail.com*

(December 29, 2014)

Running head: **fast Huygens sweeping methods**

## ABSTRACT

Multi-arrival Green's functions are essential in seismic modeling, migration and inversion. Huygens-Kirchhoff integrals provide a bridge to integrate locally valid first-arrival Green's functions into a globally valid multi-arrival Green's function. We design robust and accurate finite-difference methods to compute first-arrival traveltimes and amplitudes so that first-arrival Green's functions can be constructed rapidly. We adapt a fast butterfly algorithm to evaluate discretized Huygens-Kirchhoff integrals. The resulting fast Huygens sweeping method enjoys the following unique features: (1) it precomputes a set of local traveltime and amplitude tables; (2) it automatically takes care of caustics; (3) it constructs Green's functions of the Helmholtz equation for arbitrary frequencies and for many point sources; (4) for a fixed number of points per wavelength it constructs each Green's function in nearly optimal complexity  $O(N \log N)$  in terms of the total number of mesh points  $N$ , where the prefactor of the complexity only depends on the specified accuracy and is independent of the frequency. 2-D and 3-D examples demonstrate the performance of the method.

## INTRODUCTION

Green's functions for the Helmholtz equation in inhomogeneous media are essential for seismic modeling, migration, and inversion. However, due to the highly oscillatory nature of wave fields which induces the so-called dispersion (pollution) error (Babuška and Sauter, 2000), it is very costly and difficult for finite-difference or finite-element methods to directly solve the equation to high accuracy in the high frequency regime; consequently, some approximate methods such as one-way wave equation and geometrical-optics based asymptotics are frequently appealed.

To construct Green's functions for the Helmholtz equation using geometrical optics, one popular approach was finite-differencing eikonal equations to compute first-arrival traveltimes (Vidale, 1990; van Trier and Symes, 1991; Qin et al., 1992; Schneider et al., 1992; Hole and Zelt, 1995; Schneider, 1995; Pica, 1997; Sethian and Popovici, 1999; Kim and Cook, 1999; Franklin and Harris, 2001; Qian and Symes, 2002a,b; Tsai et al., 2003; Zhao, 2005; Zhang et al., 2005; Qian et al., 2007b,a; Kao et al., 2004; Zhang et al., 2006; Leung and Qian, 2006; Benamou et al., 2010; Alkhalifah and Fomel, 2010; Serna and Qian, 2010; Fomel et al., 2009; Luo and Qian, 2011, 2012; Luo et al., 2012). However, in Geoltrain and Brac (1993) and Gray and May (1994), prestack Kirchhoff depth migration using first-arrival Green's functions has been questioned in imaging complex structures which host multiple transmitted arrivals as the first-arrival traveltimes in complex media usually do not correspond to the most energetic traveltimes crucial for imaging complex structures (Nichols, 1994); furthermore, Geoltrain and Brac (1993) suggested to use dynamically correct multi-arrival Green's functions in which both multi-valued eikonals and amplitudes are correctly accounted for. Consequently, Operto et al. (2000) extended the asymptotic ray-Born migration/inversion originally designed to process one single arrival to the case of multiple arrivals by using ray-theory based dynamically correct multi-arrival Green's functions so as to account for the cross-contributions of all the source-receiver ray paths; naturally, it is nontrivial to construct such ray-theory Green's functions because it has to explicitly keep track of caustics, ray branches, and the KMAH index so that multi-valued phases and amplitudes are correctly taken into consideration (Cerveny et al., 1977; Chapman, 1985). As

an alternative, Gaussian beams are able to take care of multiple arrivals and caustics automatically in ray-theory asymptotics for Green’s functions at the cost of expensive beam summations (Cerveny et al., 1982; Popov, 1982; Ralston, 1983; Hill, 1990; Gray, 2005; Albertin et al., 2004; Leung et al., 2007; Tanushev et al., 2007; Hu and Stoffa, 2009; Qian and Ying, 2010a,b; Leung and Qian, 2010; Bao et al., 2014).

On the other hand, Bevc (1997) proposed a semi-recursive Kirchhoff depth migration method to image complex structures by combining wave-equation datuming (Berryhill, 1979) and first-arrival based Kirchhoff migration (Geoltrain and Brac, 1993). Bevc succeeded in obtaining accurate images of complex structures by breaking up the structure into small depth regions so that traveltimes fields emanated from point-sources located in the small depth regions do not develop the adverse effects of caustics, head waves, and multiple arrivals; correspondingly, first-arrival Green’s functions are physically correct in each small depth region so that first-arrival Kirchhoff migrations are accurate in imaging the corresponding small depth region, where Berryhill’s wave-equation datuming technique (Berryhill, 1979) is used to prepare the data for the Kirchhoff migration in each small depth region; see Li and Fomel (2013) for a recent implementation of this migration method. In fact, Bevc’s approach amounts to constructing *a kinematically correct multi-arrival Green’s functions implicitly and indirectly by using first-arrivals of Huygens secondary sources*. Given that first-arrivals are easy to compute by finite-differencing eikonal equations, a natural question is: *can we construct dynamically correct multi-arrival Green’s functions explicitly by using first-arrivals and related amplitudes of Huygens secondary sources?* Such multi-arrival Green’s functions will find wide applications not only in prestack Kirchhoff depth migrations but also in wave-equation-based migrations. Recently, Luo et al. (2014a) proposed a Eulerian geometrical-optics method, the fast Huygens sweeping method, for constructing exactly such multi-arrival Green’s functions by finite-differencing eikonal and transport equations corresponding to Huygens secondary sources and integrating physically valid, first-arrival Green’s functions of secondary sources with the Huygens-Kirchhoff integral formula (Burridge, 1962; Baker and Copson, 1987).

The idea of the fast Huygens sweeping method (Luo et al., 2014a) can be summarized as follows.

In some applications, it is reasonable to assume that geodesics (rays) have a consistent orientation so that the Helmholtz equation may be viewed as an evolution equation in one of the spatial directions. With such applications in mind, the fast Huygens sweeping method can be used for computing Green’s functions of Helmholtz equations in inhomogeneous media in the high-frequency regime and in the presence of caustics. The first novelty of the method is that the Huygens-Kirchhoff secondary source principle is used to integrate many locally valid asymptotic solutions to yield a globally valid asymptotic solution so that caustics associated with the usual geometrical-optics ansatz can be treated automatically. The second novelty is that a butterfly algorithm is adapted to carry out the matrix-vector products induced by the Huygens-Kirchhoff integration in  $O(N \log N)$  operations, where  $N$  is the total number of mesh points, and the proportionality constant depends on the desired accuracy and is independent of the frequency parameter. To reduce the storage of the resulting traveltime and amplitude tables, each table is compressed into a linear combination of tensor-product based multivariate Chebyshev polynomials so that the information of each table is encoded into a small number of Chebyshev coefficients. As a result, the method enjoys the following desired features: (1) it precomputes a set of local traveltime and amplitude tables; (2) it automatically takes care of caustics; (3) it constructs Green’s functions of the Helmholtz equation for arbitrary frequencies and for many point sources; (4) for a fixed number of points per wavelength it constructs each Green’s function in nearly optimal complexity in terms of the total number of mesh points, where the prefactor of the complexity only depends on the specified accuracy and is independent of the frequency parameter.

In this work, we further develop the fast Huygens sweeping method by designing more efficient and robust finite-difference methods for computing first-arrival traveltimes and corresponding amplitudes, and we carry out systematic comparisons between our globally valid asymptotic Green’s functions and those obtained by directly finite-differencing Helmholtz equations for various models, including the Marmousi model.

Our fast Huygens sweeping method allows both vertical and lateral variations in velocity fields as long as the velocity fields host rays with a consistent orientation such as downgoing or upgoing,

and the resulting wave field has no aperture limitation, which is different from that obtained by solving a aperture-limited one-way wave equation. In the context of fully recursive F-X migration as illustrated in Gray and May (1994), our method can be viewed as a semi-recursive F-X modeling method so that it is natural to further develop the methodology into a semi-recursive F-X migration method, and this is an ongoing project.

The paper is organized as follows. We start to present the factorization approaches and the Babich's formulation for computing phases and amplitudes so as to construct locally valid geometric-optics Green's functions. High order factorizations and approximations of phases and amplitudes near source points will be presented. Then we recall the fast Huygens-sweeping method for constructing globally valid asymptotic Green's functions. Both 2-D and 3-D numerical experiments are presented to demonstrate the performance of our methods. Concluding remarks are given at the end.

## HIGH ORDER APPROXIMATION OF EIKONAL AND AMPLITUDE

We consider the Helmholtz equation with a point-source condition in the high frequency regime,

$$\nabla_{\mathbf{r}}^2 U + \frac{\omega^2}{v^2(\mathbf{r})} U = -\delta(\mathbf{r} - \mathbf{r}_0) \quad (1)$$

with the Sommerfeld radiation condition imposed at infinity, where  $U(\mathbf{r}, \omega; \mathbf{r}_0)$  is the wave field,  $\omega$  is the frequency,  $v(\mathbf{r})$  is the wave speed,  $\mathbf{r}_0 \equiv (x_0, y_0, z_0)$  is the source point, and  $\nabla_{\mathbf{r}}^2$  denotes the Laplacian at  $\mathbf{r} \equiv (x, y, z)$ . The geometrical-optics (GO) large- $\omega$  ansatz for the Green's function with respect to a generic source  $\mathbf{r}'$ ,

$$G(\mathbf{r}, \omega; \mathbf{r}') \approx A(\mathbf{r}; \mathbf{r}') e^{i\omega\tau(\mathbf{r}; \mathbf{r}')} \text{ in 3-D, } \left( \approx \frac{1}{\sqrt{\omega}} A(\mathbf{r}; \mathbf{r}') e^{i(\omega\tau(\mathbf{r}; \mathbf{r}') + \pi/4)} \text{ in 2-D} \right) \quad (2)$$

yields the eikonal equation for phase  $\tau$  and the transport equation for amplitude  $A$ , respectively,

$$|\nabla_{\mathbf{r}}\tau| = \frac{1}{v(\mathbf{r})}, \quad \tau(\mathbf{r}'; \mathbf{r}') = 0, \quad (3)$$

$$\nabla_{\mathbf{r}} \cdot (A^2 \nabla_{\mathbf{r}} \tau) = 0, \quad A(\mathbf{r}'; \mathbf{r}') = A'(\mathbf{r}'). \quad (4)$$

Since  $\tau$  and  $A$  are locally smooth in a neighborhood of the source  $\mathbf{r}'$  excluding the source itself (Milnor, 1963; Symes and Qian, 2003), they yield a valid GO Green's function in that local neighborhood.  $\tau$  and  $A$  are weakly coupled in the sense that  $\tau$  must be computed first by solving the eikonal equation (3) and then substituted in the transport equation (4) for computing  $A$ . Since the Laplacian of  $\tau$  is involved in (4), in order to get  $l$ -th order accurate  $A$ , at least  $(l+2)$ -th order accurate  $\tau$  is required. Due to the source singularity as  $\tau$  behaves like a distance function which is non-differentiable at the source point (Qian and Symes, 2002a), computing high-order accurate  $\tau$  and  $A$  by finite-differencing equations (3) and (4) is not a trivial matter. Without special treatments of source singularities, any high-order finite-difference methods for solving (3) and (4) can formally have at most first-order accuracy and large errors.

### High-order factorization for eikonals

We first recall a factorization approach to resolving the source singularity for computing  $\tau$  (Pica, 1997; Zhang et al., 2005; Fomel et al., 2009; Luo and Qian, 2011, 2012; Luo et al., 2012). In the factorization approach,  $\tau$  is factored as

$$\tau = \tilde{\tau} \bar{\tau}, \quad (5)$$

where  $\tilde{\tau}$  is pre-determined analytically to capture the source singularity such that  $\bar{\tau}$  is the new unknown that is smooth at the source and satisfies the factored eikonal equation,

$$|\tilde{\tau} \nabla_{\mathbf{r}} \bar{\tau} + \bar{\tau} \nabla_{\mathbf{r}} \tilde{\tau}| = 1/v(\mathbf{r}). \quad (6)$$

For instance,  $\tilde{\tau}$  may be taken as  $\tilde{\tau}(\mathbf{r}; \mathbf{r}') = \frac{|\mathbf{r}-\mathbf{r}'|}{v(\mathbf{r}')}$ .

Since  $\bar{\tau}$  is smooth at the source, we can solve equation (6) efficiently with high-order Lax-Friedrichs weighted essentially non-oscillatory (LxF-WENO) schemes as designed in Kao et al. (2004); Zhang et al. (2006); Luo and Qian (2011); Luo et al. (2012). In a  $P$ -th order LxF-WENO finite difference method on a mesh of size  $h$ ,  $\bar{\tau}$  must be initialized in a neighborhood of size  $2(P-1)h$  centered at the source, and these initial values are fixed during iterations. In Luo et al. (2014b), an accurate, efficient, and systematic approach was introduced to initialize  $\bar{\tau}$  near the source. Based on the power series expansion of  $\tau^2$  which is smooth near the source, one can derive approximations of  $\tau$  near the source up to arbitrary order of accuracy.

We recall the derivation of high order approximation of  $\tau$  near the source. Assume that  $T(\mathbf{r}) \equiv \tau^2(\mathbf{r})$  and  $S(\mathbf{r}) \equiv 1/v^2(\mathbf{r})$  are analytic at the source which is set to be the origin without loss of generality. We can expand  $T$  and  $S$  as power series,

$$T(\mathbf{r}) = \sum_{\nu=0}^{\infty} T_{\nu}(\mathbf{r}), \quad S(\mathbf{r}) = \sum_{\nu=0}^{\infty} S_{\nu}(\mathbf{r}), \quad (7)$$

where  $T_{\nu}$  and  $S_{\nu}$  are homogeneous polynomials of degree  $\nu$  in  $\mathbf{r}$ . From the eikonal equation (3), we have

$$ST = \frac{1}{4} |\nabla_{\mathbf{r}} T|^2. \quad (8)$$

By substituting (7) into (8), we have

$$\left( \sum_{\nu=0}^{\infty} S_{\nu}(\mathbf{r}) \right) \left( \sum_{\nu=0}^{\infty} T_{\nu}(\mathbf{r}) \right) = \frac{1}{4} \left( \sum_{\nu=0}^{\infty} \nabla_{\mathbf{r}} T_{\nu}(\mathbf{r}) \right)^2, \quad (9)$$

from which one can derive  $\{T_{\nu}\}$  term by term by collecting terms of the same degree. Following Luo et al. (2014b), we can derive

$$T_0(\mathbf{r}) = 0, \quad T_1(\mathbf{r}) = 0, \quad T_2(\mathbf{r}) = S_0 \mathbf{r}^2,$$

and a recursive formula for computing  $T_P(\mathbf{r})$  for  $P \geq 3$ ,

$$(P-1)S_0 T_P(\mathbf{r}) = \sum_{\nu=1}^{P-2} S_\nu(\mathbf{r}) T_{P-\nu}(\mathbf{r}) - \frac{1}{4} \sum_{\nu=2}^{P-2} \nabla_{\mathbf{r}} T_{\nu+1}(\mathbf{r}) \cdot \nabla_{\mathbf{r}} T_{P-\nu+1}(\mathbf{r}). \quad (10)$$

Then we use the truncated sum  $\tilde{T}_P \equiv \sum_{\nu=2}^P T_\nu$  to approximate  $T$  near the source, and we further choose  $\tilde{\tau}_P \equiv \sqrt{\tilde{T}_P}$  to approximate  $\tau$  near the source with accuracy

$$|\tau(\mathbf{r}) - \tilde{\tau}_P(\mathbf{r})| = O(|\mathbf{r}|^P), \quad |\mathbf{r}| \rightarrow 0.$$

Taking  $\tilde{\tau}_P$  as high-order approximations of  $\tau$  near the source, we apply high-order LxF-WENO methods to solve the factored equation (6). In the  $P$ -th order LxF-WENO method for solving (6) to obtain  $\bar{\tau}$ , we first choose  $\tilde{\tau}(\mathbf{r}) \equiv \sqrt{S_0}|\mathbf{r}|$ . To initialize  $\bar{\tau}$  near the source,  $\bar{\tau}$  is assigned as 1 at the source and as  $\tilde{\tau}_P/\tilde{\tau}$  at other points in the  $2(P-1)h$  neighborhood of the source so that these values are fixed during the LxF-WENO sweeping iterations. At other points, the LxF-WENO iterations are used to update  $\bar{\tau}$  with  $\tilde{\tau}(\mathbf{r}) \equiv \sqrt{S_0}|\mathbf{r}|$ .

## High-order factorization for amplitudes

We extend the above factorization approach to deal with the amplitude  $A$  near the source. Since  $A$  is singular at the source, we introduce Babich's formulation (Babich, 1965),

$$B = A\tau^{(d-1)/2} \quad (11)$$

into the transport equation (4) for  $A$  so that we have the Babich's transport equation for the amplitude factor  $B$  (Babich, 1965),

$$\nabla_{\mathbf{r}} T(\mathbf{r}) \cdot \nabla_{\mathbf{r}} B(\mathbf{r}) + B(\mathbf{r}) \left[ \frac{1}{2} \nabla_{\mathbf{r}}^2 T(\mathbf{r}) - d/v^2(\mathbf{r}) \right] = 0, \quad (12)$$

where  $d$  is the spatial dimension and  $T(\mathbf{r}) = \tau^2(\mathbf{r})$ . Since the amplitude factor  $B$  is smooth near and at the source (Babich, 1965) while the original amplitude  $A$  is singular at the source, we will use this transport equation to derive high order approximations of  $B$  near the source. In addition to power series expansions in (7), we assume that  $B$ 's power series expansion is given as

$$B(\mathbf{r}) = \sum_{\nu=0}^{\infty} B_{\nu}(\mathbf{r}), \quad (13)$$

where  $B_{\nu}$  are homogeneous polynomials of degree  $\nu$  in  $\mathbf{r}$ . It follows that  $B_{\nu}$  can be determined term by term by substituting (13) into (12):

$$\left( \sum_{\nu=2}^{\infty} \nabla_{\mathbf{r}} T_{\nu}(\mathbf{r}) \right) \cdot \left( \sum_{\nu=1}^{\infty} \nabla_{\mathbf{r}} B_{\nu}(\mathbf{r}) \right) + \left( \sum_{\nu=0}^{\infty} B_{\nu}(\mathbf{r}) \right) \left[ \frac{1}{2} \left( \sum_{\nu=2}^{\infty} \nabla_{\mathbf{r}}^2 T_{\nu}(\mathbf{r}) \right) - d \left( \sum_{\nu=0}^{\infty} S_{\nu}(\mathbf{r}) \right) \right] = 0. \quad (14)$$

We know from Babich (1965) that

$$B_0 = \frac{1}{2\sqrt{2\pi}} \text{ for } d = 2, \text{ and } B_0 = \frac{\sqrt{S_0}}{4\pi} \text{ for } d = 3.$$

Comparing the linear terms in (14) and using the homogeneity of  $B_1$ , we have

$$\begin{aligned} & \nabla_{\mathbf{r}} T_2 \cdot \nabla_{\mathbf{r}} B_1 + \frac{1}{2} (B_0 \nabla_{\mathbf{r}}^2 T_3 + B_1 \nabla_{\mathbf{r}}^2 T_2) - d(B_0 S_1 + B_1 S_0) = 0, \\ \Rightarrow & 2S_0 \mathbf{r} \cdot \nabla_{\mathbf{r}} B_1 + \frac{1}{2} (B_0 \nabla_{\mathbf{r}}^2 T_3 + 2B_1 d S_0) - d(B_0 S_1 + B_1 S_0) = 0, \\ \Rightarrow & 2S_0 B_1 + \frac{1}{2} B_0 \nabla_{\mathbf{r}}^2 T_3 - d B_0 S_1 = 0, \\ \Rightarrow & B_1 = \frac{1}{2S_0} \left( -\frac{1}{2} B_0 \nabla_{\mathbf{r}}^2 T_3 + d B_0 S_1 \right). \end{aligned} \quad (15)$$

Equating  $P$ -th degree terms on both sides of (14), we have

$$B_P = \frac{1}{2PS_0} \left( - \sum_{\nu=1}^{P-1} \nabla_{\mathbf{r}} B_{\nu}(\mathbf{r}) \cdot \nabla_{\mathbf{r}} T_{P+2-\nu}(\mathbf{r}) - \frac{1}{2} \sum_{\nu=0}^{P-1} B_{\nu}(\mathbf{r}) \nabla_{\mathbf{r}}^2 T_{P+2-\nu}(\mathbf{r}) + d \sum_{\nu=0}^{P-1} B_{\nu}(\mathbf{r}) S_{P-\nu}(\mathbf{r}) \right). \quad (16)$$

Consequently, we can now use the truncated sum to approximate  $B$ , i.e.,

$$\tilde{B}_P \equiv \sum_{\nu=0}^P B_\nu, \quad (17)$$

and

$$|\tilde{B}_P - B| = O(|\mathbf{r}|^P), \quad |\mathbf{r}| \rightarrow 0.$$

Taking  $\tilde{B}_P$  as high-order approximation of  $B$  near the source, we will apply high-order LxF-WENO methods to solve the Babich's transport equation (12) for  $B$ . In the  $P$ -th order LxF-WENO method for solving (12),  $B$  is assigned as  $\tilde{B}_P$  in the  $2(P-1)h$ -neighborhood of the source so that these values are fixed during the LxF-WENO iterations; at other points, the LxF-WENO iterations are used to update  $B$ .

Comparing to the adaptive mesh refinement method for treating the source singularity used in Kim and Cook (1999); Qian and Symes (2002a), high-order factorization based high-order LxF-WENO sweeping methods make computing high-order accurate  $\bar{\tau}$  and  $B$  easy and efficient, resulting in high-order accurate  $\tau$  and  $A$  and locally valid first-arrival Green's functions. If one is satisfied with accurate first-arrival Green's functions, then the schemes developed above suffice. However, since in general one needs multi-arrival Green's functions, we incorporate these first-arrival Green's functions into the fast Huygens sweeping method introduced in Luo et al. (2014a) to build globally valid multi-arrival Green's functions.

## HUYGENS-PRINCIPLE BASED GLOBALLY VALID GREEN'S FUNCTIONS

Assume that a domain  $\Omega$  is illuminated by an exterior source  $\mathbf{r}_0 \notin \Omega$ , and  $\mathcal{S} = \partial\Omega$  is the closed surface enclosing the domain  $\Omega$ ; see Figure 1(a). At any observation point  $\mathbf{r} \in \Omega$ , the wave field  $U(\mathbf{r}; \mathbf{r}_0)$  excited by the source  $\mathbf{r}_0$  can be written as the Huygens-Kirchhoff (HK) integral over  $\mathcal{S}$

(Burridge, 1962; Baker and Copson, 1987):

$$\begin{aligned}
U(\mathbf{r}; \mathbf{r}_0) &= \int_{\mathcal{S}} \{G(\mathbf{r}'; \mathbf{r}) \nabla_{\mathbf{r}'} U(\mathbf{r}'; \mathbf{r}_0) \cdot \mathbf{n}(\mathbf{r}') - U(\mathbf{r}'; \mathbf{r}_0) \nabla_{\mathbf{r}'} G(\mathbf{r}'; \mathbf{r}) \cdot \mathbf{n}(\mathbf{r}')\} dS(\mathbf{r}') \\
&= \int_{\mathcal{S}} \{G(\mathbf{r}; \mathbf{r}') \nabla_{\mathbf{r}'} U(\mathbf{r}'; \mathbf{r}_0) \cdot \mathbf{n}(\mathbf{r}') - U(\mathbf{r}'; \mathbf{r}_0) \nabla_{\mathbf{r}'} G(\mathbf{r}; \mathbf{r}') \cdot \mathbf{n}(\mathbf{r}')\} dS(\mathbf{r}'),
\end{aligned} \tag{18}$$

where  $G(\mathbf{r}; \mathbf{r}') = G(\mathbf{r}'; \mathbf{r})$  by reciprocity,  $\mathbf{n}(\mathbf{r}')$  is the outward normal to  $\mathcal{S}$  at  $\mathbf{r}' = (x', y', z')$ , and  $G(\mathbf{r}; \mathbf{r}')$  is the Green's function associated with the source  $\mathbf{r}'$ . In the integral,  $G(\mathbf{r}; \mathbf{r}')$  and  $\nabla_{\mathbf{r}'} G(\mathbf{r}; \mathbf{r}') \cdot \mathbf{n}(\mathbf{r}')$  associated with  $\mathbf{r}'$  on  $\mathcal{S}$  can be approximated with the GO ansatz (2).

By retaining the leading order term after substituting (2) into (18), we have

$$\begin{aligned}
U(\mathbf{r}; \mathbf{r}_0) &\approx \int_{\mathcal{S}} \{G(\mathbf{r}; \mathbf{r}') [\nabla_{\mathbf{r}'} U(\mathbf{r}'; \mathbf{r}_0) \cdot \mathbf{n}(\mathbf{r}')] - G(\mathbf{r}; \mathbf{r}') \nabla_{\mathbf{r}'} \tau(\mathbf{r}; \mathbf{r}') \cdot \mathbf{n}(\mathbf{r}') [i\omega U(\mathbf{r}'; \mathbf{r}_0)]\} dS(\mathbf{r}') \\
&\approx \int_{\mathcal{S}} \{G(\mathbf{r}; \mathbf{r}') [\nabla_{\mathbf{r}'} U(\mathbf{r}'; \mathbf{r}_0) \cdot \mathbf{n}(\mathbf{r}')] - G(\mathbf{r}; \mathbf{r}') \cos(\theta(\mathbf{r}; \mathbf{r}')) [i\omega U(\mathbf{r}'; \mathbf{r}_0)/v(\mathbf{r}')]\} dS(\mathbf{r}'),
\end{aligned} \tag{19}$$

where  $\theta$  is the takeoff angle of the ray from source  $\mathbf{r}'$  to receiver  $\mathbf{r}$  and is constant along the ray, i.e.,

$$\nabla_{\mathbf{r}} \theta(\mathbf{r}; \mathbf{r}') \cdot \nabla_{\mathbf{r}} \tau(\mathbf{r}; \mathbf{r}') = 0; \tag{20}$$

consequently,

$$\nabla_{\mathbf{r}} \cos(\theta(\mathbf{r}; \mathbf{r}')) \cdot \nabla_{\mathbf{r}} \tau(\mathbf{r}; \mathbf{r}') = 0. \tag{21}$$

Since the first-arrival GO approximations of Green's functions associated with the secondary sources are valid only locally, (19) can only be used in a narrow band near  $\mathcal{S}$  so that rays emanating from the source have not developed caustics yet. Hence the fast Huygens sweeping method carries out the integration (19) in a layer by layer manner; see Figure 1(b) and Figure 2. The secondary sources are placed on the top boundary of each layer, and the HK integral (19) is performed inside each layer.

## Layer-based Huygens sweeping

We recall the planar-layer based Huygens sweeping method (Luo et al., 2014a) as illustrated in Figure 1(b) and Figure 2 and summarized as follows.

### Algorithm: Algorithmic sketch for Huygens sweeping method

- **Stage 1 (offline).** Precompute asymptotic ingredients such as phases, amplitudes, and takeoff angles. Since these ingredients only depend on the velocity and do not depend on wavelength or frequency, these can be computed on very coarse meshes by using high-order schemes. We carry out the following steps: (1) the whole computational domain is partitioned into layers as in Figure 1(b) so that rays emanating from the primary source and each secondary source have not developed caustics yet; (2) the tables of phases, amplitudes and takeoff angles with respect to the primary source in the first layer (see Figure 2(a)) and those tables for each secondary source located on the layer boundary of the other layers (see Figure 2(b)) are computed by solving the relevant equations as described above with high-order LxF-WENO methods in the corresponding layer; and (3) these tables are compressed with the Chebyshev expansion based data compression technique (Alkhalifah, 2011; Boyd, 2001; Luo et al., 2014a); see Appendix A.
- **Stage 2 (online).** Given a frequency  $\omega$ , we specify four to six (4 to 6) points per wavelength so that the wavefield is sampled with  $n$  mesh points along each dimension: (1) in the first layer containing the primary source, construct the first-arrival Green's function with tables of the primary source; see Figure 2(a); (2) from the second layer to all the other layers, for each line of secondary sources on the layer boundary, tables of phases, amplitudes and takeoff angles are read from the hard drive and used to reconstruct the tables on the underlying mesh by Chebyshev sums (see Appendix A); if necessary the tables are interpolated with respect to the secondary sources onto the underlying mesh; and (3) the HK integral (19) is then discretized with a numerical quadrature rule, such as the trapezoidal rule as used in

the current work, and the resulting matrix-vector products are evaluated by a fast butterfly algorithm as shown in Luo et al. (2014a); see Figure 2(b).

## Complexity analysis

In the above algorithm, two sets of different meshes are involved in the computation. One set of meshes is used for computing GO ingredients; since these ingredients are independent of wavelength or frequency, these meshes are independent of wavelength as well and can be very coarse so that high-order schemes still can yield sufficiently accurate GO ingredients. The other set of meshes is used to sample the wavefield. Since we need to specify four to six points per wavelength to resolve wave oscillations, these meshes depend on wavelength or frequency. Therefore, the following complexity analysis treats the two sets of meshes differently.

Assume that there are  $L$  layers in the partition. In **Stage 1**, the complexity of computing each table in each layer with LxF-WENO methods is  $O(m^{d-1}(m/L) \log m)$ , where  $m$  mesh points are used for each spatial direction and the  $\log m$  factor comes from the number of sweeping iterations. Since there are  $O(m^{d-1})$  secondary sources for each layer, the total complexity of computing all the tables for secondary sources is  $LO(m^{d-1}(m^{d-1}(m/L) \log m)) = O(m^{2d-1} \log m)$ , which is analogous to the computational complexity for asymptotic ingredients in phase space (Symes and Qian, 2003; Leung et al., 2007; Luo et al., 2014a). Since these tables are precomputed and are independent of wavelength or frequency, those tables can be computed on very coarse meshes by using high-order schemes and can be reused for different frequencies.

In **Stage 2**, direct evaluation of the HK-integral induced matrix-vector products is computationally expensive. To accelerate the evaluation, we adapt a multilevel matrix decomposition based butterfly algorithm originated in Michielssen and Boag (1996) and further developed in O’Neil (2007); Candés et al. (2009); Hu et al. (2013); Luo et al. (2014a). Following Luo et al. (2014a), given frequency  $\omega$ , four to six points are specified per wavelength so that the wavefield is sampled with  $n$  mesh points along each spatial direction. For each layer, the complexity of the butterfly

algorithm is  $O(n^{d-1}(n/L) \log(n^{d-1}(n/L))) = O((N/L) \log N)$ , where  $N = O(n^d)$  and the prefactor is independent of frequency  $\omega$ ; the complexity of Chebyshev sums and interpolation with respect to secondary sources is  $O(N/L)$ , where the prefactor depends on the number of spectral coefficients in the truncated Chebyshev expansion. The number of spectral coefficients is considered to be much smaller than  $O(n)$ . Therefore, the total complexity of constructing the wavefield in the whole domain is  $O(N \log N)$ . Please refer to Luo et al. (2014a) for more implementation details of the fast butterfly algorithm used here.

Once the data tables are pre-computed, the fast Huygens sweeping method can be used to construct the global wave field with  $O(N \log N)$  complexity for a given primary source and for an arbitrary given frequency. Moreover, the data tables can be reused for many different primary sources. For different primary sources, only the tables with respect to the primary sources inside the first layer are recomputed. The tables of the other layers are reused. Therefore, we refer **Stage 1** as “**offline**” and **Stage 2** as “**online**”. These unique merits are much desired in many applications, such as seismic imaging and inversion.

## NUMERICAL EXAMPLES

We present several numerical experiments to demonstrate our new method. We denote the coarse mesh in Stage 1 as GO mesh. We choose  $P = 3$  in the high-order factorization for computing  $\tau$  and  $B$ . The mesh for sampling wavefields is chosen such that a fixed number of points (4 to 6 points) per wavelength are used to resolve wave oscillations. We compare our numerical solutions with those obtained by a direct solver on a much finer mesh. For the direct finite-difference Helmholtz solver, we use a nine-point stencil (Jo et al., 1996) instead of the usual five-point stencil to reduce dispersion errors and obtain more reliable wave fields; the perfectly-matched-layer (PML) absorbing boundary conditions are also imposed (Berenger, 1994). The resulting sparse linear system is solved by the sparse LU solver in the Matlab platform.

## Example 1: Two-dimensional Sinusoidal velocity model

In this example the velocity is chosen as

$$v = 1 + 0.2 \sin(3\pi(x + 0.05)) \sin(0.5\pi z) \text{ (km/s)},$$

on the domain  $[0, 1] \times [0, 2]$  (km). In Stage 1, the GO coarse mesh is  $101 \times 201$ , and the asymptotic ingredients are compressed with ratio  $50 : 1$ . In Stage 2, the separation distance  $d_f$  between the sources and receivers is fixed as 0.1 (km).

Figure 3 shows the contour plots of the numerical solutions obtained by our approach and the direct Helmholtz solver mentioned above with  $\omega = 32\pi$ . Our approach uses approximately 5 points per wavelength while the direct solver uses approximately 40 points per wavelength. Figure 4 shows comparisons between the solutions. Table 1 shows the efficiency and stability of our method and comparisons between the butterfly algorithm and direct summation.

Figure 5 shows numerical solutions by our method and the direct solver with a different setup, where the domain is  $[0, 1] \times [0, 3]$  (km) and the source is at  $(0.5, 1.5)$ (km).

## Example 2: Synthetic Marmousi velocity model

In this example we construct wavefields for the Marmousi model. The original model is sampled on a 0.024km by 0.024 (km) grid, consisting of 384 samples in the  $x$ -direction and 122 samples in the  $z$ -direction; therefore the domain is  $[0, 9.192] \times [0, 2.904]$  (km). Since we need high-order derivatives of the velocity in high-order approximations, the velocity is smoothed by solving the following least-squares regularization problem,

$$\min_{v(\mathbf{r})} \{|v(\mathbf{r}) - v^m(\mathbf{r})|^2 + \alpha |\nabla_{\mathbf{r}} v(\mathbf{r})|^2 + \beta |\nabla_{\mathbf{r}}^2 v(\mathbf{r})|^2\},$$

where  $v^m$  is the original Marmousi model,  $\alpha$  and  $\beta$  are smoothness parameters. We choose  $\alpha = \beta = 10^{-4}$ . Figure 6 shows the Marmousi models. We first test a case with the smoothed velocity. The velocity field is a sampled window from receivers 218 to 313 (96 receivers in total) in the smoothed Marmousi model. The windowed domain is  $[5.208, 7.488] \times [0, 2.904]$  (km). In Stage 1, the GO coarse mesh is  $96 \times 122$  and the asymptotic ingredients are compressed with ratio 25 : 1. In Stage 2, the separation distance  $d_f$  between the sources and receivers is fixed as 0.192 (km).

We apply our new algorithm to the smoothed Marmousi velocity model as in Figure 6(b). This synthetic geological structure creates many strong and localized velocity heterogeneities. Figure 7 shows the wave fields with the primary source point given as (5.380, 0.24) (km) and  $\omega = 32\pi$  by two different methods, where the fast Huygens sweeping method uses a mesh of  $286 \times 364$  points and the direct Helmholtz solver uses a mesh of  $1711 \times 2179$  points. To apply the direct Helmholtz solver on the fine mesh, the velocity field on the original coarse mesh is interpolated onto the finer mesh first with spline interpolations.

Next we choose a sampled window from receivers 41 to 158 of the Marmousi model where the velocity is only slightly smoothed; see Figure 8. The windowed domain is  $[0, 2.904] \times [0.96, 3.768]$  (km). In Stage 1, the GO coarse mesh is  $118 \times 122$  and the data compression ratio for asymptotic ingredients is 25 : 1. In Stage 2, the separation distance  $d_f$  between the sources and receivers is fixed as 0.192 (km).

Figure 9 shows the wave fields with the primary source point given as (1.488, 0.48) (km) and  $\omega = 32\pi$  by the two methods, where the fast Huygens sweeping method uses a mesh of  $352 \times 364$  points and the direct Helmholtz solver uses a mesh of  $2107 \times 2179$  points. To apply the direct Helmholtz solver on the fine mesh, the velocity field on the original coarse mesh is interpolated onto the finer mesh first with spline interpolations.

### Example 3: Three-dimensional Vinje velocity model (Vinje et al., 1996)

In the example the velocity is chosen as

$$v = 3.0 - 1.75e^{(-((x-1)^2+(y-1)^2+(z-1)^2)/0.64)} \text{ (km/s)},$$

on the domain  $[0, 2] \times [0, 2] \times [0, 2]$  (km). In Stage 1, the GO coarse mesh is  $51 \times 51 \times 51$ , and the data compression ratio for asymptotic ingredients is  $32 : 1$ . In Stage 2, the separation distance  $d_f$  between the sources and receivers is fixed as 0.3 (km).

We partition the 3-D domain into two layers at the plane  $z = 1.2$  (km). When  $\omega = 32\pi$ , there are roughly 26 waves propagating in each direction. If a direct solver is used to compute the wave field, then the number of unknowns is roughly 17 millions if 10 points per wavelength is used to capture each wave, resulting in a huge linear system to deal with, not to mention the fact that whether 10 points per wavelength suffice or not. To use our fast Huygens sweeping method, we choose approximately 4 points per wavelength.

Figure 10 shows the results for different primary sources. The tables corresponding to the primary source in the first layer need to be recomputed for different primary sources. Tables with respect to those secondary sources do not need to be recomputed. Table 2 shows the running times of our method for different  $\omega$ 's.

## CONCLUSION

We have developed the fast Huygens sweeping method for evaluating the Huygens-Kirchhoff integral so that locally valid first-arrival Green's functions can be integrated into a globally valid multi-arrival Green's function. The needed ingredients for constructing first-arrival Green's functions, such as first-arrival traveltimes and amplitudes, were computed by utilizing a set of newly developed tools, such as the factorization approach, the Babich's formulation, power-series based high-order approximations, and high-order LxF-WENO methods. The Huygens-Kirchhoff integral

were evaluated by adapting a fast butterfly algorithm so that the fast Huygens sweeping method has computational complexity  $O(N \log N)$ , where  $N$  is the total number of mesh points, and the proportionality constant depends on the desired accuracy and is independent of frequency. Numerical examples demonstrated performance, efficiency, and accuracy of the proposed method.

### ACKNOWLEDGMENT

The authors would like to thank the assistant editor Dr. Jeffrey Shragge, the associate editor, Dr. Samuel Gray and the reviewers for constructive comments that improve this work significantly. Qian is supported by NSF-1222368. Luo is supported by NSF DMS-1418908.

## APPENDIX A

### COMPRESSION WITH CHEBYSHEV EXPANSION

We illustrate the compression process for a 3-D traveltime table. The same can be done for amplitude and takeoff angle tables, and for 2-D tables (Boyd, 2001; Alkhalifah, 2011). Without loss of generality, we assume that the traveltime  $\tau(\mathbf{r}; \mathbf{r}_0)$  is defined on  $[-1, 1]^3$  for a given source point  $\mathbf{r}_0$ .  $\tau$  can be expanded in terms of Chebyshev polynomials of the first kind (Boyd, 2001),

$$\tau(\mathbf{r}; \mathbf{r}_0) = \tau(x, y, z; \mathbf{r}_0) = \sum_{m=0}^{\infty} \sum_{n=0}^{\infty} \sum_{k=0}^{\infty} C_{mnk}(\mathbf{r}_0) T_m(x) T_n(y) T_k(z), \quad (\text{A-1})$$

where  $T_l(\cdot)$  is the Chebyshev polynomial of the first kind and of order  $l$ :  $T_l(\cdot) = \cos(l \cos^{-1}(\cdot))$ ; and  $\{C_{mnk}(\mathbf{r}_0)\}$  are spectral coefficients. To determine  $\{C_{mnk}(\mathbf{r}_0)\}$ , we use the computed traveltime on the coarse mesh in Stage 1.  $\{C_{mnk}(\mathbf{r}_0)\}$  are then computed with the fast Fourier cosine transform (Boyd, 2001; Alkhalifah, 2011). In numerical applications, for given accuracy it is enough to keep only the first few coefficients among  $\{C_{mnk}(\mathbf{r}_0)\}$ ,

$$\tau(\mathbf{r}; \mathbf{r}_0) = \tau(x, y, z; \mathbf{r}_0) \approx \sum_{m=0}^{C_X-1} \sum_{n=0}^{C_Y-1} \sum_{k=0}^{C_Z-1} C_{mnk}(\mathbf{r}_0) T_m(x) T_n(y) T_k(z), \quad (\text{A-2})$$

with  $C_X$ ,  $C_Y$  and  $C_Z$  being given numbers. Instead of saving  $\tau$  on the coarse mesh, the set of significant coefficients,

$$\tilde{C} = \{C_{mnk}(\mathbf{r}_0) : 0 \leq m \leq C_X - 1, 0 \leq n \leq C_Y - 1, 0 \leq k \leq C_Z - 1\},$$

will be saved for later use. In practice, it is possible to reconstruct  $\tau$  with high accuracy even with a relatively high compression ratio defined as (the size of the coarse mesh)/( $C_X C_Y C_Z$ ).

With  $\tilde{C}$ , the traveltime on any specified computational mesh can be computed by evaluating the formula (A-2) on that mesh as product of low-rank matrices, which is detailed below by using *Matlab* notation:

- In 3-D,  $\tau$  on a mesh of size  $M \times N \times K$  spanned by  $\mathbf{X} = [-1 : h_x : 1]$ ,  $\mathbf{Y} = [-1 : h_y : -1]$ , and  $\mathbf{Z} = [-1 : h_z : 1]$  is reconstructed by

$$\tau = \text{permute}(\text{permute}(\mathbf{T}'_{\mathbf{X}} \tilde{\mathbf{C}} \mathbf{T}_{\mathbf{Z}}, [1 \ 3 \ 2]) \mathbf{T}_{\mathbf{Y}}, [1 \ 3 \ 2]),$$

where  $\mathbf{T}_{\mathbf{X}}$ ,  $\mathbf{T}_{\mathbf{Y}}$ , and  $\mathbf{T}_{\mathbf{Z}}$  are of size  $C_X \times M$ ,  $C_Y \times N$ , and  $C_Z \times K$  respectively, and

$$\mathbf{T}_{\mathbf{X}}(l, :) = T_{l-1}(\mathbf{X}), \quad \mathbf{T}_{\mathbf{Y}}(l, :) = T_{l-1}(\mathbf{Y}), \quad \text{and} \quad \mathbf{T}_{\mathbf{Z}}(l, :) = T_{l-1}(\mathbf{Z}).$$

- In 2-D,  $\tau$  on a 2-D mesh of size  $M \times K$  spanned by  $\mathbf{X} = [-1 : h_x : 1]$  and  $\mathbf{Z} = [-1 : h_z : 1]$  is reconstructed as

$$\tau = \mathbf{T}'_{\mathbf{X}} \tilde{\mathbf{C}} \mathbf{T}_{\mathbf{Z}},$$

where  $\tilde{\mathbf{C}}$  is of size  $C_X \times C_Z$ .

## REFERENCES

- Albertin, U., D. Yingst, P. Kitchenside, and V. Tcheverda, 2004, True-amplitude beam migration, *in* 74th Ann. Internat. Mtg., Soc. Expl. Geophys., Expanded Abstracts: Soc. Expl. Geophys., 949–952.
- Alkhalifah, T., 2011, Efficient travelttime compression for 3D prestack Kirchhoff migration: *Geophys. Prosp.*, **69**, 1–9.
- Alkhalifah, T., and S. Fomel, 2010, An eikonal-based formulation for travelttime perturbation with respect to the source location: *Geophysics*, **75**, T175–T183.
- Babich, V. M., 1965, The short wave asymptotic form of the solution for the problem of a point source in an inhomogeneous medium: *USSR Computational Mathematics and Mathematical Physics*, **5**, 247–251.
- Babuška, I. M., and S. A. Sauter, 2000, Is the pollution effect of the FEM avoidable for the Helmholtz equation considering high wave numbers?: *SIAM Review*, **42**, 451–484.
- Baker, B., and E. T. Copson, 1987, *The mathematical theory of Huygens' principle*: Ams Chelsea Publishing.
- Bao, G., J. Lai, and J. Qian, 2014, Fast multiscale Gaussian beam methods for wave equations in bounded domains: *J. Comput. Phys.*, **261**, 36–64.
- Benamou, J. D., S. Luo, and H.-K. Zhao, 2010, A Compact Upwind Second Order Scheme for the Eikonal Equation: *J. Comput. Math.*, **28**, 489–516.
- Berenger, J.-P., 1994, A perfectly matched layer for the absorption of electromagnetic waves: *J. Comput. Phys.*, **114**, 185–200.
- Berryhill, J. R., 1979, Wave-equation datuming: *Geophysics*, **44**, 1329–1344.
- Bevc, D., 1997, Imaging complex structures with semirecursive Kirchhoff migration: *Geophysics*, **62**, 577–588.
- Boyd, J. P., 2001, *Chebyshev and Fourier Spectral Methods*: Second edition, Dover, New York.
- Burridge, R., 1962, The reflexion of high-frequency sound in a liquid sphere: *Proc. Roy. Soc. Ser. A*, **270**, 144–154.

- Candés, E., L. Demanet, and L. Ying, 2009, A fast butterfly algorithm for the computation of Fourier integral operators: *Multiscale Modeling & Simulation*, **7**, 1727–1750.
- Cerveny, V., I. A. Molotkov, and I. Psencik, 1977, *Ray method in seismology*: Univerzita Karlova press.
- Cerveny, V., M. Popov, and I. Psencik, 1982, Computation of wave fields in inhomogeneous media-Gaussian beam approach: *Geophys. J. R. Astr. Soc.*, **70**, 109–128.
- Chapman, C. H., 1985, Ray theory and its extensions: WKB and Maslov seismogram: *J. Geophys.*, **58**, 27–43.
- Fomel, S., S. Luo, and H.-K. Zhao, 2009, Fast sweeping method for the factored eikonal equation: *J. Comput. Phys.*, **228**, 6440–6455.
- Franklin, J., and J. M. Harris, 2001, A high-order fast marching scheme for the linearized eikonal equation: *J. Comput. Acoustics*, **9**, 1095–1109.
- Geoltrain, S., and J. Brac, 1993, Can we image complex structures with first-arrival traveltimes: *Geophysics*, **58**, 564–575.
- Gray, S., 2005, Gaussian beam migration of common shot records: *Geophysics*, **70**, S71–S77.
- Gray, S., and W. May, 1994, Kirchhoff migration using eikonal equation traveltimes: *Geophysics*, **59**, 810–817.
- Hill, N., 1990, Gaussian beam migration: *Geophysics*, **55**, 1416–1428.
- Hole, J., and B. C. Zelt, 1995, 3-D finite-difference reflection traveltimes: *Geophys. J. Internat.*, **121**, 427–434.
- Hu, C., and P. Stoffa, 2009, Slowness-driven Gaussian-beam prestack depth migration for low-fold seismic data: *Geophysics*, **74**, WCA35–WCA45.
- Hu, J., S. Fomel, L. Demanet, and L. Ying, 2013, A fast butterfly algorithm for generalized Radon transforms: *Geophysics*, **78**, U41–U51.
- Jo, C.-H., C. Shin, and J. H. Suh, 1996, An optimal 9-point, finite-difference, frequency-space, 2-D scalar wave extrapolator: *Geophysics*, **61**, 529–537.
- Kao, C. Y., S. Osher, and J. Qian, 2004, Lax-Friedrichs sweeping schemes for static Hamilton-Jacobi

- equations: *J. Comput. Phys.*, **196**, 367–391.
- Kim, S., and R. Cook, 1999, 3-D traveltimes computation using second-order ENO scheme: *Geophysics*, **64**, 1867–1876.
- Leung, S., and J. Qian, 2006, An adjoint state method for three-dimensional transmission traveltimes tomography using first-arrivals: *Comm. Math. Sci.*, **4**, 249–266.
- , 2010, The backward phase flow and FBI-transform-based Eulerian Gaussian beams for the Schrödinger equation: *J. Comput. Phys.*, **229**, 8888–8917.
- Leung, S., J. Qian, and R. Burrige, 2007, Eulerian Gaussian beams for high-frequency wave propagation: *Geophysics*, **72**, SM61–SM76.
- Li, S., and S. Fomel, 2013, Kirchhoff migration using eikonal-based computation of traveltimes source derivative: *Geophysics*, **78**, S211–S219.
- Luo, S., and J. Qian, 2011, Factored singularities and high-order Lax-Friedrichs sweeping schemes for point-source traveltimes and amplitudes: *J. Comput. Phys.*, **230**, 4742–4755.
- , 2012, Fast sweeping methods for factored anisotropic eikonal equations: multiplicative and additive factors: *J. Sci. Comput.*, **52**, 360–382.
- Luo, S., J. Qian, and R. Burrige, 2014a, Fast Huygens sweeping methods for Helmholtz equations in inhomogeneous media in the high frequency regime: *J. Comput. Phys.*, **270**, 378–401.
- , 2014b, High-order factorization based high-order hybrid fast sweeping methods for point-source Eikonal equations: *SIAM J. Numer. Anal.*, **52**, 23–44.
- Luo, S., J. Qian, and H.-K. Zhao, 2012, Higher-order schemes for 3-D traveltimes and amplitudes: *Geophysics*, **77**, T47–T56.
- Michielssen, E., and A. Boag, 1996, A multilevel matrix decomposition algorithm for analysing scattering from large structures: *IEEE Trans. Antennas Propagat.*, **44**, no. 8, 1086–1093.
- Milnor, J., 1963, *Morse Theory*: Princeton Univ. Press.
- Nichols, D., 1994, *Imaging complex structures using band limited Green’s functions*: PhD thesis, Stanford University, Stanford, CA94305.
- O’Neil, M., 2007, *A new class of analysis-based fast transforms*: Doctoral Dissertation, Yale Uni-

versity.

- Operto, S., S. Xu, and G. Lambare, 2000, Can we image quantitatively complex models with rays: *Geophysics*, **65**, 1223–1238.
- Pica, A., 1997, Fast and accurate finite-difference solutions of the 3D eikonal equation parametrized in celerity: 67th Ann. Internat. Mtg, Soc. of Expl. Geophys., 1774–1777.
- Popov, M. M., 1982, A new method of computation of wave fields using Gaussian beams: *Wave Motion*, **4**, 85–97.
- Qian, J., and W. W. Symes, 2002a, An adaptive finite-difference method for traveltimes and amplitudes: *Geophysics*, **67**, 167–176.
- , 2002b, Finite-difference quasi-P traveltimes for anisotropic media: *Geophysics*, **67**, 147–155.
- Qian, J., and L. Ying, 2010a, Fast Gaussian wavepacket transforms and Gaussian beams for the Schrödinger equation: *J. Comput. Phys.*, **229**, 7848–7873.
- , 2010b, Fast multiscale Gaussian wavepacket transforms and multiscale Gaussian beams for the wave equation: *SIAM J. Multiscale Modeling and Simulation*, **8**, 1803–1837.
- Qian, J., Y.-T. Zhang, and H.-K. Zhao, 2007a, A fast sweeping methods for static convex Hamilton-Jacobi equations: *J. Sci. Comput.*, **31(1/2)**, 237–271.
- , 2007b, Fast sweeping methods for eikonal equations on triangulated meshes: *SIAM J. Numer. Anal.*, **45**, 83–107.
- Qin, F., Y. Luo, K. B. Olsen, W. Cai, and G. T. Schuster, 1992, Finite difference solution of the eikonal equation along expanding wavefronts: *Geophysics*, **57**, 478–487.
- Ralston, J., 1983, Gaussian beams and the propagation of singularities. *Studies in partial differential equations*. MAA Studies in Mathematics, 23. Edited by W. Littman. pp.206-248.
- Schneider, W. A. J., 1995, Robust and efficient upwind finite-difference traveltime calculations in three dimensions: *Geophysics*, **60**, 1108–1117.
- Schneider, W. A. J., K. Ranzinger, A. Balch, and C. Kruse, 1992, A dynamic programming approach to first arrival traveltime computation in media with arbitrarily distributed velocities: *Geophysics*, **57**, 39–50.

- Serna, S., and J. Qian, 2010, A stopping criterion for higher-order sweeping schemes for static Hamilton-Jacobi equations: *J. Comput. Math.*, **28**, 552–568.
- Sethian, J. A., and A. M. Popovici, 1999, 3-D traveltime computation using the fast marching method: *Geophysics*, **64**, 516–523.
- Symes, W. W., and J. Qian, 2003, A slowness matching Eulerian method for multivalued solutions of eikonal equations: *J. Sci. Comp.*, **19**, 501–526.
- Tanushev, N., J. Qian, and J. Ralston, 2007, Mountain waves and Gaussian beams: *SIAM J. Multiscale Modeling and Simulation*, **6**, 688–709.
- Tsai, Y.-H., L.-T. Cheng, S. Osher, and H.-K. Zhao, 2003, Fast sweeping algorithms for a class of Hamilton-Jacobi equations: *SIAM J. Numer. Anal.*, **41**, 673–694.
- van Trier, J., and W. W. Symes, 1991, Upwind finite-difference calculation of traveltimes: *Geophysics*, **56**, 812–821.
- Vidale, J. E., 1990, Finite-difference calculation of traveltimes in three dimensions: *Geophysics*, **55**, 521–526.
- Vinje, V., E. Iversen, K. Astebol, and H. Gjoystdal, 1996, Estimation of multivalued arrivals in 3d models using wavefront construction - part I: *Geophysical Prospecting*, **44**, 819–842.
- Zhang, L., J. W. Rector, and G. M. Hoversten, 2005, Eikonal solver in the celerity domain: *Geophysical Journal International*, **162**, 1–8.
- Zhang, Y. T., H. K. Zhao, and J. Qian, 2006, High order fast sweeping methods for static Hamilton-Jacobi equations: *J. Sci. Comp.*, **29**, 25–56.
- Zhao, H.-K., 2005, A fast sweeping method for eikonal equations: *Math. Comput.*, **74**, 603–627.

## LIST OF FIGURES

1 2-D demonstration of the H-K integral and partition of the domain into layers: (a) H-K integral with  $\mathcal{S}$  an infinite plane; and (b) partition of the domain into planar layers. Star represents the primary source.

2 Receivers and sources in the H-K integral and illustration of the fast Huygens sweeping algorithm. Larger star represents the primary source; little stars represent the secondary sources on the boundary of each layer; the grid represents the mesh. In offline Stage 1, the coarse mesh is used. In online Stage 2, the refined mesh is used and depends on  $\omega$ . The region of size  $d_f$  is independent of  $\omega$ . (a) shows the first layer with respect to the primary source; and (b) shows a layer  $l$  with  $l > 1$  and with respect to secondary sources on the boundary of this layer.

3 Real part of the wave field for the sinusoidal model. (a) obtained by our method (mesh  $101 \times 201$ , solid black lines indicating the locations of secondary sources for each layer) and (b) obtained by the direct Helmholtz solver (mesh  $801 \times 1601$ ).  $\omega = 32\pi$ . The primary source point is  $(0.5, 0.2)$ (km).

4 Real part of the wave field for the sinusoidal model. Comparisons between the solutions obtained by our method and the direct Helmholtz solver at (a)  $z = 0.55$  and (b)  $z = 1.75$  (km), respectively. Solid lines represent solutions by the direct Helmholtz solver; circles represent solutions by our method ( $p = 9$ ).  $\omega = 32\pi$ . The primary source point is  $(0.5, 0.2)$ (km).

5 Real part of the wave field for the sinusoidal model. (a) obtained by our method (mesh  $101 \times 301$  and solid black lines indicating the locations of secondary sources for each layer) and (b) obtained by the direct Helmholtz solver (mesh  $801 \times 2401$ ).  $\omega = 32\pi$ . The primary source point is  $(0.5, 1.5)$ (km).

6 Marmousi model. (a) the original Marmousi velocity field and (b) the smoothed velocity field. The region between two black lines is the sampled window from receivers 218 to 313.

7 Smoothed Marmousi model with velocity in Figure 6. Real part of the wave field with (a) obtained by our method and (b) obtained by the direct Helmholtz solver. Solid lines show the positions of the secondary sources. (c)-(d) are comparisons of the solutions at  $z = 1.472, 2.592$ (km),

respectively, where circles represent the solution by our method and solid lines represent the solution by the direct Helmholtz solver.

8 Marmousi model with (a) the original Marmousi velocity field and (b) a slightly smoothed velocity field. The region between two black lines is the sampled window from receivers 41 to 158.

9 Smoothed Marmousi model with velocity in Figure 8. Real part of the wave field with (a) obtained by our method and (b) obtained by the direct Helmholtz solver. Solid lines show the positions of the secondary sources. (c)-(d) are comparisons of the solutions at  $x = 2.640, 3.360(\text{km})$ , respectively, where circles represent the solution by our method and solid lines represent the solution by the direct Helmholtz solver.

10 The Vinje model. Wavefields are constructed by our method on a mesh  $101 \times 101 \times 101$  with  $\omega = 32\pi$ . In (a), (b) and (c), the primary point source is  $(0.6, 0.6, 0.24)$  (km); and in (d)(e)(f), the primary source is  $(1.4, 1.4, 0.36)$  (km). (a), (b) and (c) show the real part of the wavefields at  $x = 0.6(\text{km})$ ,  $y = 0.6(\text{km})$ , and  $z = 1.8(\text{km})$ , respectively; and (d), (e), and (f) show the real part of the wavefields at  $x = 1.4(\text{km})$ ,  $y = 1.4(\text{km})$ , and  $z = 1.8(\text{km})$ , respectively.

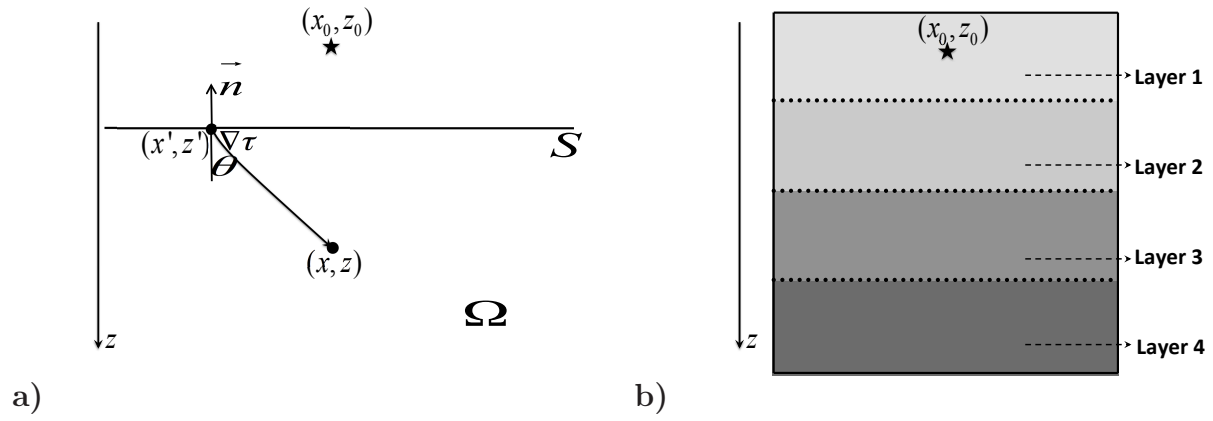


Figure 1: 2-D demonstration of the H-K integral and partition of the domain into layers: (a) H-K integral with  $\mathcal{S}$  an infinite plane; and (b) partition of the domain into planar layers. Star represents the primary source.

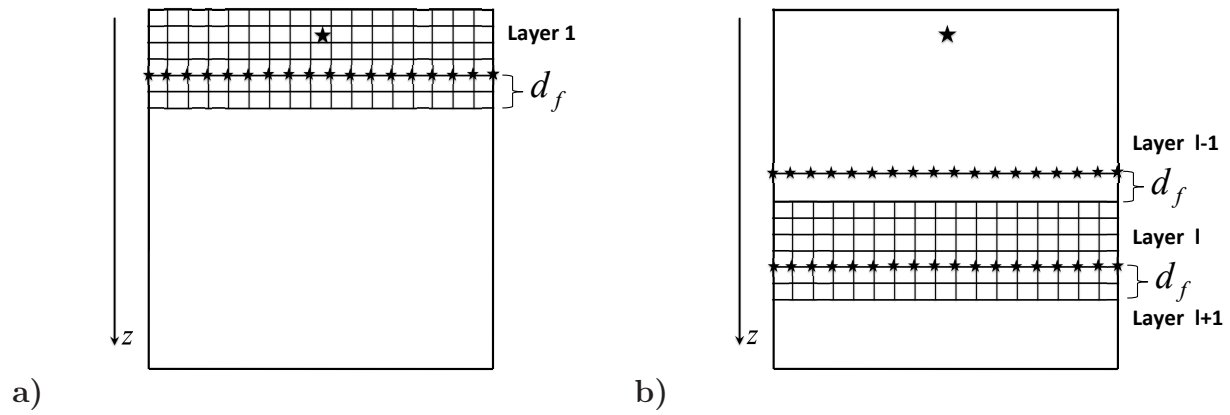


Figure 2: Receivers and sources in the H-K integral and illustration of the fast Huygens sweeping algorithm. Larger star represents the primary source; little stars represent the secondary sources on the boundary of each layer; the grid represents the mesh. In offline Stage 1, the coarse mesh is used. In online Stage 2, the refined mesh is used and depends on  $\omega$ . The region of size  $d_f$  is independent of  $\omega$ . (a) shows the first layer with respect to the primary source; and (b) shows a layer  $l$  with  $l > 1$  and with respect to secondary sources on the boundary of this layer.

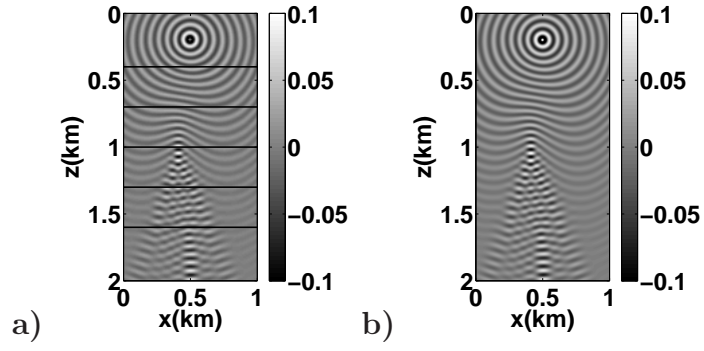


Figure 3: Real part of the wave field for the sinusoidal model. (a) obtained by our method (mesh  $101 \times 201$ , solid black lines indicating the locations of secondary sources for each layer) and (b) obtained by the direct Helmholtz solver (mesh  $801 \times 1601$ ).  $\omega = 32\pi$ . The primary source point is  $(0.5, 0.2)$ (km).

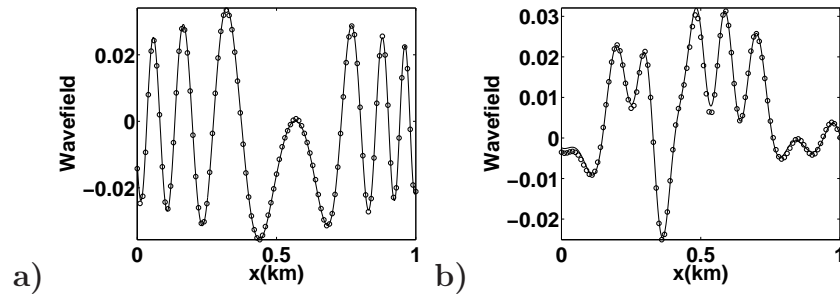


Figure 4: Real part of the wave field for the sinusoidal model. Comparisons between the solutions obtained by our method and the direct Helmholtz solver at (a)  $z = 0.55$  and (b)  $z = 1.75$  (km), respectively. Solid lines represent solutions by the direct Helmholtz solver; circles represent solutions by our method ( $p = 9$ ).  $\omega = 32\pi$ . The primary source point is  $(0.5, 0.2)$ (km).

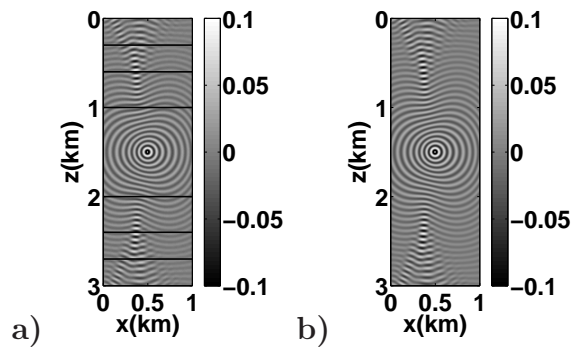
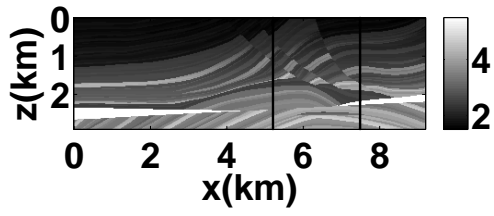
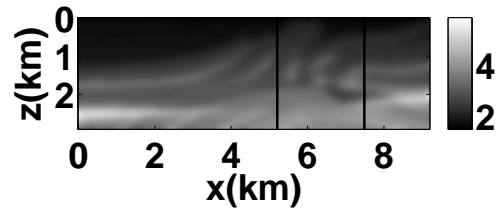


Figure 5: Real part of the wave field for the sinusoidal model. (a) obtained by our method (mesh  $101 \times 301$  and solid black lines indicating the locations of secondary sources for each layer) and (b) obtained by the direct Helmholtz solver (mesh  $801 \times 2401$ ).  $\omega = 32\pi$ . The primary source point is  $(0.5, 1.5)(\text{km})$ .



a)



b)

Figure 6: Marmousi model. (a) the original Marmousi velocity field and (b) the smoothed velocity field. The region between two black lines is the sampled window from receivers 218 to 313.

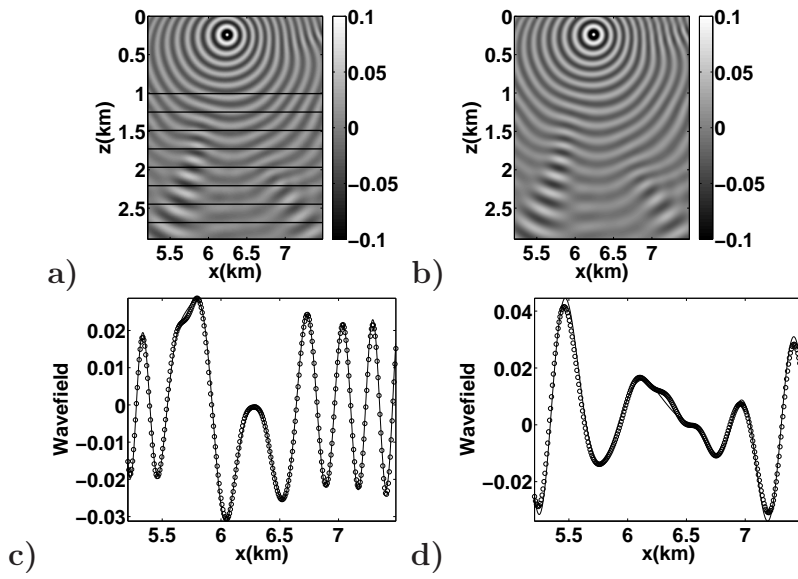
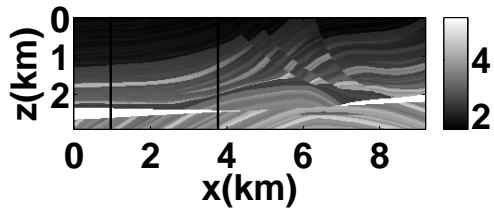
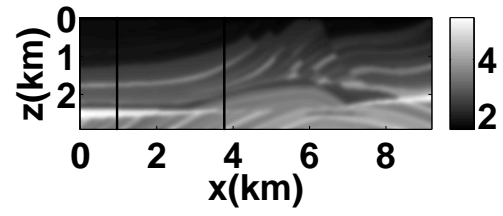


Figure 7: Smoothed Marmousi model with velocity in Figure 6. Real part of the wave field with (a) obtained by our method and (b) obtained by the direct Helmholtz solver. Solid lines show the positions of the secondary sources. (c)-(d) are comparisons of the solutions at  $z = 1.472, 2.592$ (km), respectively, where circles represent the solution by our method and solid lines represent the solution by the direct Helmholtz solver.



a)



b)

Figure 8: Marmousi model with (a) the original Marmousi velocity field and (b) a slightly smoothed velocity field. The region between two black lines is the sampled window from receivers 41 to 158.

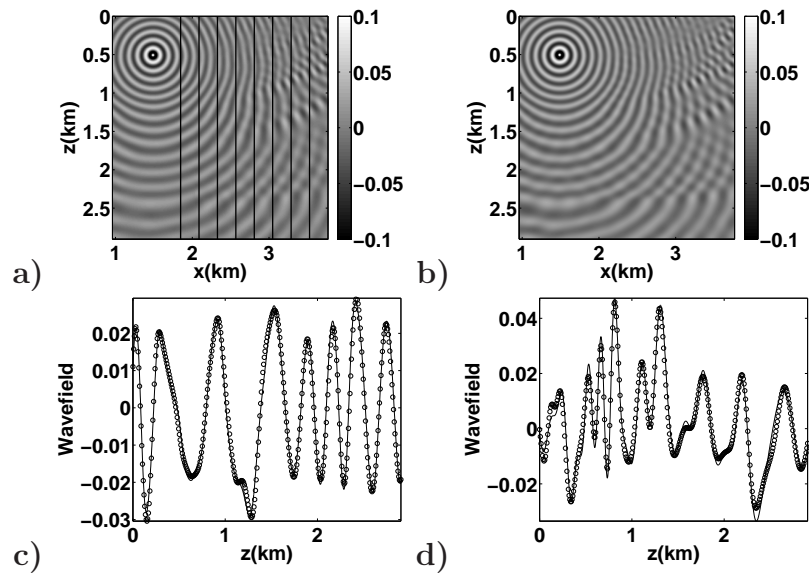


Figure 9: Smoothed Marmousi model with velocity in Figure 8. Real part of the wave field with (a) obtained by our method and (b) obtained by the direct Helmholtz solver. Solid lines show the positions of the secondary sources. (c)-(d) are comparisons of the solutions at  $x = 2.640, 3.360(\text{km})$ , respectively, where circles represent the solution by our method and solid lines represent the solution by the direct Helmholtz solver.

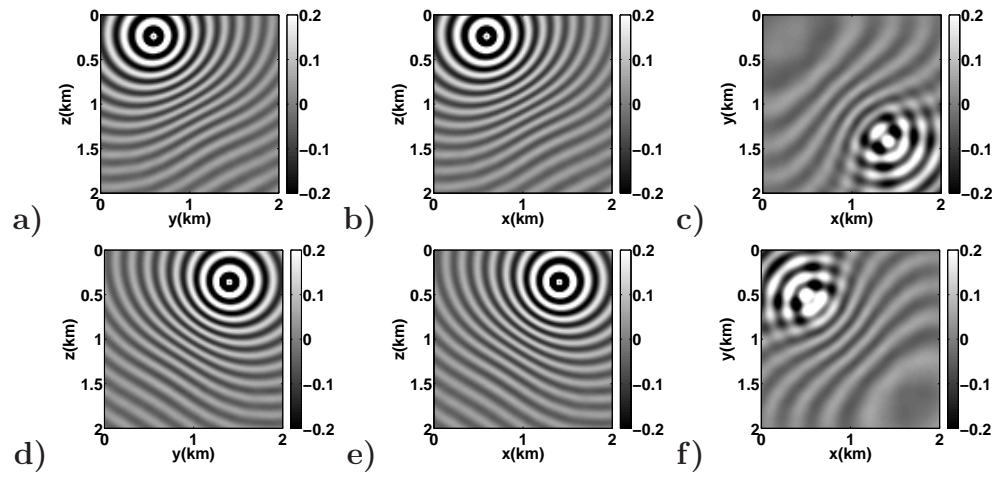


Figure 10: The Vinje model. Wavefields are constructed by our method on a mesh  $101 \times 101 \times 101$  with  $\omega = 32\pi$ . In (a), (b) and (c), the primary point source is  $(0.6, 0.6, 0.24)$  (km); and in (d)(e)(f), the primary source is  $(1.4, 1.4, 0.36)$  (km). (a), (b) and (c) show the real part of the wavefields at  $x = 0.6$ (km),  $y = 0.6$ (km), and  $z = 1.8$ (km), respectively; and (d), (e), and (f) show the real part of the wavefields at  $x = 1.4$ (km),  $y = 1.4$ (km), and  $z = 1.8$ (km), respectively.

## LIST OF TABLES

1 Sinusoidal model. Numerical accuracy and comparisons on CPUtime (seconds) between the butterfly-algorithm based Huygens-Kirchhoff summation (denoted as  $T_M$ ) and the direct Huygens-Kirchhoff summation (denoted as  $T_D$ ) in the second layer.  $p = 9$  Chebyshev nodes are used in each dimension. The source point is  $(0.5, 0.2)$ (km). NPW denotes the number of points per wavelength.

2 Vinje model. CPUtime in seconds for the butterfly-algorithm based Huygens-Kirchhoff summation.  $p = 7, 9, 11$  Chebyshev nodes are used in each dimension. Source point is  $(1.0, 1.0, 0.2)$  (km). NPW denotes the number of points per wavelength.

Mesh	$201 \times 61$	$401 \times 121$	$801 \times 241$	$1601 \times 481$	$3201 \times 961$	$6401 \times 1921$
$\omega/2\pi$	32	64	128	256	512	1024
NPW	5	5	5	5	5	5
$T_D$ (sec)	0.28	1.48	13.12	100.84	810.60	6503.15
$p = 9$						
$L_2$ (abs)	1.43E-5	6.03E-6	4.06E-6	4.03E-6	2.65E-6	2.37E-6
$L_2$ (rel)	1.34E-3	7.98E-4	7.62E-4	1.07E-3	9.99E-4	1.26E-3
$T_M$ (sec)	0.61	1.55	4.69	18.30	66.43	299.67
$T_D/T_M$	0.46	0.95	2.80	5.51	12.20	21.70

Table 1: Sinusoidal model. Numerical accuracy and comparisons on CPUtime (seconds) between the butterfly-algorithm based Huygens-Kirchhoff summation (denoted as  $T_M$ ) and the direct Huygens-Kirchhoff summation (denoted as  $T_D$ ) in the second layer.  $p = 9$  Chebyshev nodes are used in each dimension. The source point is (0.5, 0.2)(km). NPW denotes the number of points per wavelength.

Mesh	$101 \times 101 \times 101$	$201 \times 201 \times 201$
$\omega/2\pi$	16	32
NPW	4	4
$T_M$ (sec) (p=7)	194.36	1404.61
$T_M$ (sec) (p=9)	328.72	2555.59
$T_M$ (sec) (p=11)	625.60	4843.46

Table 2: Vinje model. CPUtime in seconds for the butterfly-algorithm based Huygens-Kirchhoff summation.  $p = 7, 9, 11$  Chebyshev nodes are used in each dimension. Source point is (1.0, 1.0, 0.2) (km). NPW denotes the number of points per wavelength.